Simulations of pilot-wave dynamics in a simple harmonic potential

Kristin M. Kurianski,[1] Anand U. Oza,[2] and John W. M. Bush[1,*]
[1]*Department of Mathematics, Massachusetts Institute of Technology, Cambridge, Massachusetts 02139, USA*
[2]*Courant Institute of Mathematical Sciences, New York University, New York, New York 10012, USA*
(Received 22 April 2017; published 14 November 2017)

We present the results of a numerical investigation of droplets walking in a harmonic potential on a vibrating fluid bath. The droplet's trajectory is described by an integro-differential equation, which is simulated numerically in various parameter regimes. We produce a regime diagram that summarizes the dependence of the walker's behavior on the system parameters for a droplet of fixed size. At relatively low vibrational forcing, a number of periodic and quasiperiodic trajectories emerge. In the limit of large vibrational forcing, the walker's trajectory becomes chaotic, but the resulting trajectories can be decomposed into portions of unstable quasiperiodic states.

DOI: 10.1103/PhysRevFluids.2.113602

I. INTRODUCTION

A droplet can bounce indefinitely on the surface of a fluid bath that is vibrating vertically with acceleration $\gamma\cos(2\pi ft)$ [1]. We denote by γ_F the Faraday threshold, or the forcing acceleration required to excite standing Faraday waves on the surface of the bath [2]. Below this threshold ($\gamma < \gamma_F$), the surface of the bath remains undisturbed in the absence of the drop. Beyond the bouncing threshold γ_B, specifically for $\gamma_B < \gamma < \gamma_F$, a thin air layer sustained between the drop and the bath during impact prevents coalescence. The impact imparts vertical momentum to the descending drop, reversing its direction. In the bouncing regime, the drop lands on the crest of the wave generated from its previous bounces and experiences a purely vertical force from the bath. Beyond the walking threshold γ_W, specifically for $\gamma_B < \gamma_W < \gamma < \gamma_F$, the static bouncing state gives way to a walking state [3,4]. When the droplet lands, it experiences a force with a horizontal component proportional to the slope of the surface. Consequently, the droplet walks horizontally across the surface of the bath, propelled by its own wave field.

For a bouncer to become a walker, the droplet must bounce at half the driving frequency of the bath, commensurate with the frequency of the most unstable (subharmonic) mode of the Faraday instability [4]. The walker then moves in resonance with its guiding or pilot-wave field. Each impact locally excites Faraday waves, with wavelength λ_F prescribed by the standard water-wave dispersion relation, which then affect the walker's subsequent trajectory. The lifetime of these waves increases as γ approaches γ_F and is prescribed by the memory parameter $M_e = T_d/T_F(1-\gamma/\gamma_F)$, where T_d is the decay time of the waves in the absence of forcing and T_F is the Faraday period. Thus, the walker has an associated path memory that increases as γ approaches γ_F [5].

The walkers are notable in that they exhibit several phenomena reminiscent of quantum mechanical systems. While claims of single-particle diffraction and interference [6] have been contested [7], tunneling [8,9], orbital quantization in both a rotating frame [10–12] and harmonic potential [13,14], and wavelike statistics in confined geometries [15–18] are all robust quantumlike phenomena. This hydrodynamic pilot-wave system and its relation to realist quantum theories, specifically, de Broglie's double-solution pilot-wave theory [19] and its modern extensions [20], were recently reviewed by Bush [21,22].

Fort *et al.* [10] demonstrated that when a droplet walks in a rotating frame, its inertial orbits become approximately quantized owing to the droplet's interaction with its own wave field. Oza *et al.* [11] and Harris and Bush [12] revisited this system theoretically and experimentally, respectively.

*Corresponding author: bush@math.mit.edu

Linear stability analysis of the orbital pilot-wave solutions provided rationale for the emergence of orbital quantization, as was manifest in bands of accessible orbital radii [11]. When the circular orbits destabilized, a variety of periodic, quasiperiodic, and chaotic trajectories emerged [23]. In the chaotic regime, it was found that coherent statistical structure emerged in a trajectory's local loop radius. In both numerical simulations and experiments, the histograms of the loop radius had maxima corresponding to the zeros of the Bessel function $J_0(k_F r)$, where $k_F = 2\pi/\lambda_F$ is the Faraday wave number. This suggests that walkers in the chaotic regime tend to make loops quantized on half the Faraday wavelength, roughly corresponding to the radii of the unstable circular orbits [11]. Thus, the statistics of a walker in the chaotic regime are dictated by the relative instability of the underlying unstable orbital states.

We here present the results of a numerical investigation of droplets walking in the presence of a central force. This work was inspired by the ingenious experiments of Perrard *et al.* [13] and Labousse *et al.* [24], in which a walking droplet containing ferrofluid was subjected to an applied central force $\boldsymbol{F} = -k\boldsymbol{x}$, where k is the spring constant and $\boldsymbol{x}$ is the displacement from the symmetry axis. In their experiments, Perrard *et al.* [13] demonstrated that the walker dynamics is highly dependent on the memory parameter M_e. As memory was increased progressively, predominantly stable circular orbits gave way to periodic and quasiperiodic trajectories, many of which exhibited a double quantization of mean angular momentum and mean radius. At high forcing acceleration, chaotic trajectories emerged and dominated the dynamics. The authors showed that these chaotic trajectories could be decomposed into the various unstable periodic states apparent at lower M_e with intermediate transients [13]. This decomposition suggests that, in the chaotic regime, the walker switches between unstable periodic orbits, the result being the emergence of a coherent statistical behavior. Perrard *et al.* [25] showed that chaotic trajectories found in experiments are characterized by transitions between unstable periodic orbits. At high memory, the number of possible states increased. A map of first return between successive maxima in radial extent revealed that the chaotic trajectories essentially switch between circular orbits and lemniscates [25]. Labousse *et al.* [24] identified a separation in time scales to theoretically rationalize the self-organization of walkers and the appearance of coherent structures within the dynamics. We here explore the walker's chaotic dynamics in our numerical simulations and adopt the methodology of Durey and Milewski [26] in seeking evidence of double quantization in the chaotic regime.

Labousse *et al.* [14] investigated the linear stability of circular orbits executed by a walker subject to a harmonic force. At low values of M_e, circular orbits were found to be linearly stable for all values of the initial radius [14], which is consistent with the experimental results of Perrard *et al.* [13]. As M_e was progressively increased, discrete bands of accessible stable radii emerged, separated by linearly unstable regions. These unstable regions represent solutions that can destabilize via nonoscillatory or oscillatory instabilities [14]. While the linear theory agreed well with experiments in the stable regions, it often incorrectly predicted oscillatory instabilities. This discrepancy may be rationalized in terms of stabilizing effects present in experiments that were not captured by the theory [14]. Specifically, the stabilizing influence of a variable bouncing phase has recently been demonstrated for orbiting walker pairs [27].

The transitions to chaos for walkers in the presence of Coriolis, linear spring, and Coulomb forces were characterized theoretically by Tambasco *et al.* [28]. It was shown that walking droplets subject to either a Coriolis or Coulomb force transition to chaotic trajectories via a standard period-doubling cascade while walking droplets in a simple harmonic potential transition in a manner akin to the Ruelle-Takens-Newhouse route to chaos [28]. In our work we will focus on walkers in the presence of a linear spring force and explore further the dynamics in both the periodic and chaotic regimes.

Our simulations are based on the stroboscopic model of horizontal walker dynamics developed by Oza *et al.* [29], which is rooted in the theoretical framework of pilot-wave hydrodynamics developed by Moláček and Bush [30,31]. The stroboscopic model was developed by time averaging the force balance over the bouncing period, resulting in an integro-differential equation. Milewski *et al.* [32] and Blanchette [33] developed models for pilot-wave dynamics based on weakly viscous quasipotential wave generation and evolution. Direct comparison with measurements of surface

wave profiles emphasized the importance of spatial damping in recovering the wave field far from impact [34]. The effects of spatial damping were incorporated into the stroboscopic model and shown to be important in the stability of orbiting walker pairs [27]. We proceed by implementing numerical simulations using the stroboscopic model with spatial damping in order to explore the dynamics of a walker in a harmonic potential.

Durey and Milewski [26] developed a model to analyze a variety of walking droplet systems, including a walker in a harmonic potential. To analyze the chaotic high-memory regime, the authors introduced a K-means clustering approach. Specifically, a chaotic trajectory was divided into subtrajectories corresponding to segments between successive local maxima in the trajectory's radius. The mean radius $\overline{R}$ and mean angular momentum $\overline{L}_z$ were calculated along each subtrajectory and transposed to a single point in the $(\overline{L}_z, \overline{R})$ plane. Well-separated clusters formed for each chaotic trajectory, which motivated the application of K-means clustering [26]. The centroids of each cluster were then combined on a separate plot for varying spring constant k and showed an approximate double quantization in $\overline{L}_z$ and $\overline{R}$ [26]. Their study raised the intriguing possibility that the double quantization reported by Perrard *et al.* [13] is more pronounced in the chaotic than the periodic regime. We here implement the K-means clustering technique in order to explore the statistical structure underlying the chaotic regime.

In Sec. II we briefly summarize our theoretical model. In Sec. III we provide a broad overview of the parameter space explored, indicating the regimes in which a variety of periodic, quasiperiodic, and chaotic trajectories are observed. In Sec. IV we detail several of the periodic and quasiperiodic trajectories and their associated speed, radial extent, and angular momentum. Section V focuses on a discussion of double quantization in both the periodic and chaotic regimes. We conclude with a discussion of our results and future directions in Sec. VI.

II. MODEL

The numerical investigation presented herein is based on the stroboscopic model for walker dynamics introduced by Oza *et al.* [29] combined with an improved wave field model that incorporates spatial damping [27]. A summary of the model is presented here, while the details of its derivation are presented by Moláček and Bush [30,31] and Oza *et al.* [29]. We consider a droplet of mass m and radius R_d walking on the surface of a vertically vibrating fluid bath. The bath is vibrated with forcing acceleration $\gamma\cos(2\pi ft)$ and the droplet is assumed to bounce in resonance with the subharmonic frequency $f/2$. The droplet is subjected to the external harmonic potential associated with the force $\boldsymbol{F} = -k\boldsymbol{x}_p$, where $\boldsymbol{x}_p = [x_p(t), y_p(t)]$ is the position of the droplet at time t and k is the spring constant. The horizontal motion of the drop can be described by averaging the vertical dynamics over the bouncing period T_F. The resulting trajectory equation describes the horizontal dynamics:

$$m\ddot{\boldsymbol{x}}_p + D\dot{\boldsymbol{x}}_p = -mg\nabla h(\boldsymbol{x}_p, t) - k\boldsymbol{x}_p, \tag{1}$$

where D is the time-averaged drag coefficient and g is the gravitational acceleration. The wave field is prescribed by the deflection of the bath's free surface:

$$h(\boldsymbol{x}, t) = \frac{A}{T_F}\int_{-\infty}^{t} J_0(k_F|\boldsymbol{x} - \boldsymbol{x}_p(s)|)e^{-\alpha|\boldsymbol{x}-\boldsymbol{x}_p(s)|^2/(t-s)}e^{-(t-s)/T_F M_e}ds. \tag{2}$$

Here $k_F = 2\pi/\lambda_F$ is the wave number of the most unstable Faraday wave and can be calculated numerically or approximated by the solution to the standard water-wave dispersion relation $(\pi f)^2 = (gk + \sigma k_F^3/\rho)\tanh k_F H$ [29,31]. The parameter A is the peak wave amplitude after a single impact and α is the spatial damping coefficient [27]. All relevant variables are listed in Table I and additional details may be found in Ref. [31].

The key control parameter in our simulations is the memory parameter $M_e = T_d/T_F(1 - \gamma/\gamma_F)$, which prescribes the longevity of the wave field. Effectively, we vary γ/γ_F to explore a range of M_e, since T_d and T_F are constant for a given bath of silicone oil driven at a frequency f. Physical parameters are chosen to correspond to walkers of radius $R_d = 0.37$ mm and silicone oil

TABLE I. Variables present in trajectory equations (1) and (2) and quantities of interest (3) and (4).

Variables	Definition
$\boldsymbol{x}_p(t) = [x_p(t), y_p(t)]$	Drop position
$u(t) = \lvert\dot{\boldsymbol{x}}_p(t)\rvert$	Speed of walker along trajectory
u_0	Free rectilinear walking speed
m and R_d	Drop mass and drop radius
(ν_e) ν	(Effective [31]) fluid kinematic viscosity
σ	Fluid surface tension
ρ and ρ_a	Fluid density and air density
μ_a	Air dynamic viscosity
g	Gravitational acceleration
γ	Forcing acceleration
γ_F	Faraday instability threshold
f	Forcing frequency
$T_F = 2/f$	Faraday period
$T_d \approx \frac{\lambda_F^2}{8\pi^2\nu}$	Decay time of waves in absence of vibration
λ_F and k_F	Faraday wavelength and wave number
Φ	Mean phase of wave during contact
k and $T_s = \sqrt{m/k}$	Spring constant and spring time
$D = 0.17mg\sqrt{\frac{\rho R_d}{\sigma}} + 6\pi\mu_a R_d(1 + \frac{\rho_a g R_d}{12\mu_a f})$	Drag coefficient
$\mathrm{Bo} = \frac{\rho g}{k_F^2\sigma}$	Bond number
$A = \frac{\sqrt{8\pi\nu_e T_F}}{3}\frac{(k_F R_d)^3}{3\,\mathrm{Bo}^{-1}+1}$	Wave amplitude
$F = \sqrt{\frac{1.5795\nu}{2\pi T_F}}\frac{mgk_F^4}{3k_F^2\sigma+\rho g}mgT_F\sin\Phi$	Wave force coefficient
$\alpha = \frac{\epsilon^2}{2\nu_e(1+2\epsilon^2)}$ where $\epsilon = \frac{2\pi f k_F \nu_e}{g(3\,\mathrm{Bo}^{-1}+1)}$	Wave spatial damping coefficient
$M_e = \frac{T_d}{T_F(1-\gamma/\gamma_F)}$ and $T_M = T_F M_e$	Memory parameter and memory time
$\kappa = \frac{m}{DT_F M_e}$	Nondimensional mass
$\beta = \frac{Fk_F T_F M_e^2}{D}$	Nondimensional wave force coefficient
$\chi = \frac{T_F M_e k}{D}$	Nondimensional spring constant

of viscosity 20 cS driven at a frequency of $f = 80$ Hz, roughly consistent with the experiments of Perrard *et al.* [13]. The dimensionless trajectory equation is solved numerically using a fourth-order Adams-Bashforth method for the time stepping in Eq. (1) combined with Simpson's rule for the integration in Eq. (2) [23]. Each trajectory is initialized as a bouncer at the origin $\boldsymbol{x}_p(t) = [0,0]$ for $t < 0$. This system is sensitive to initial conditions, as the walker selects an orbit based on its history. For example, if initializing the walker in a circle, circular trajectories become more common. Throughout this presentation, we maintain the choice of initializing as a bouncer at the center.

The trajectory depends on the spring constant k and the forcing acceleration γ/γ_F, which prescribes the walker's path memory. Varying both k and γ/γ_F gives rise to a variety of periodic, quasiperiodic, and chaotic orbits that will be detailed in the following sections. We give particular attention to characterizing the dependence on k and γ/γ_F of the mean nondimensional radius defined by

$$\overline{R} = \left\langle \frac{|\boldsymbol{x}_p(t)|}{\lambda_F} \right\rangle \tag{3}$$

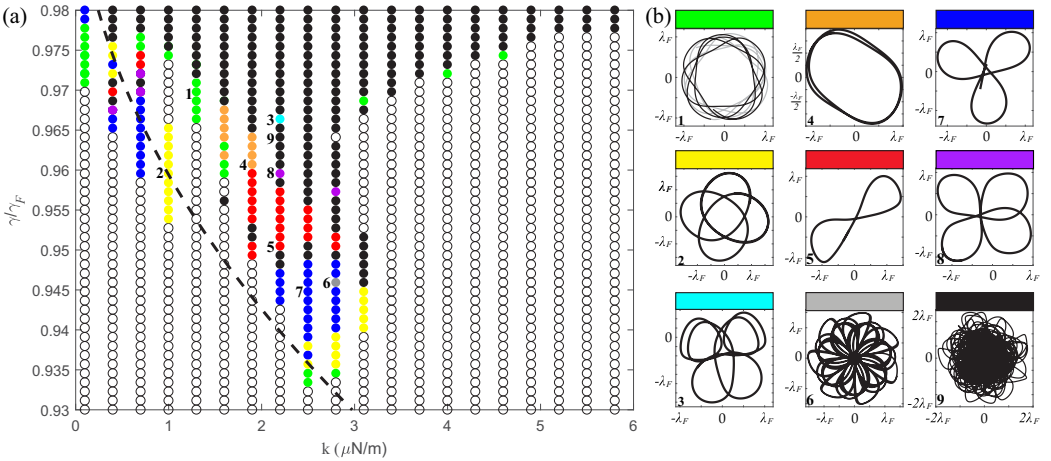

FIG. 1. (a) Dependence of simulated trajectories on vibrational forcing γ/γ_F and dimensional spring constant k over the range $0.93 \leqslant \gamma/\gamma_F \leqslant 0.98$ and $0.1 \leqslant k \leqslant 5.8$ μN/m with resolution $\Delta(\gamma/\gamma_F) = 0.0016$ and $\Delta k = 0.3$ μN/m. Open circles correspond to stable circular orbits and black closed circles to chaotic trajectories. Colored circles denote the various periodic and quasiperiodic orbits categorized in (b). The numbers in (a) correspond to the specific trajectories in (b). The dashed line denotes the locus of the curve $\sqrt{m/k} = T_d/(1-\gamma/\gamma_F)$, above which the memory time exceeds the characteristic crossing or orbital time $T_M > T_s$.

and mean nondimensional angular momentum defined by

$$\overline{L}_z = \left\langle \frac{L}{m\lambda_F V} \right\rangle = \left\langle \frac{\boldsymbol{x}_p}{\lambda_F} \times \frac{\dot{\boldsymbol{x}}_p}{V} \right\rangle, \tag{4}$$

where $\langle q \rangle$ denotes the time average of q over the entire trajectory and $V = \langle |\dot{\boldsymbol{x}}_p| \rangle$ is the mean speed.

III. REGIME DIAGRAM

We here explore the dependence of walker trajectories on the system parameters, namely, forcing acceleration γ/γ_F and dimensional spring constant k. In the absence of the wave field, balancing the centripetal acceleration ($\sim mV^2/R$) and the spring force ($\sim kR$) gives the dimensionless width of the potential well $\Lambda = (V\sqrt{m/k})/\lambda_F \sim R/\lambda_F$. As the linear stability of circular orbits in a harmonic potential was examined by Labousse *et al.* [14], the focus of this paper is on the nonlinear regime characterized by complex periodic, quasiperiodic, and chaotic dynamics.

Our numerical exploration is summarized in Fig. 1. Each color in parameter space corresponds to a particular type of trajectory. Open circles denote stable circular orbits. Green circles correspond to wobbling trajectories characterized by a periodic oscillation in orbital radius $|\boldsymbol{x}_p|$. Orange circles correspond to the stadiumlike ellipses reported in the experiments of Perrard *et al.* [13]. Blue and red circles represent trefoils and lemniscates, respectively, as were also highlighted in the experiments [13]. Yellow, purple, cyan, and gray circles correspond to more complex periodic and quasiperiodic trajectories that were not reported by Perrard *et al.* [13]. We note that these trajectories reside in relatively narrow regions of parameter space that may be difficult to access in a laboratory setting. Black circles denote chaotic dynamics in which no coherent periodic structure is apparent. We note that the majority of the periodic and quasiperiodic trajectories may be characterized in terms of either wobbling circular orbits or wobbling and precessing periodic rectilinear motion.

We consider a range of forcing accelerations $0.93 \leqslant \gamma/\gamma_F \leqslant 0.98$ consistent with that considered by Perrard *et al.* [13]. For spring constant $0.1 \leqslant k \leqslant 5.8$ μN/m, all circular orbits are stable for $\gamma/\gamma_F < 0.932$. At moderate spring constant $1 < k < 3$ μN/m and moderate forcing acceleration

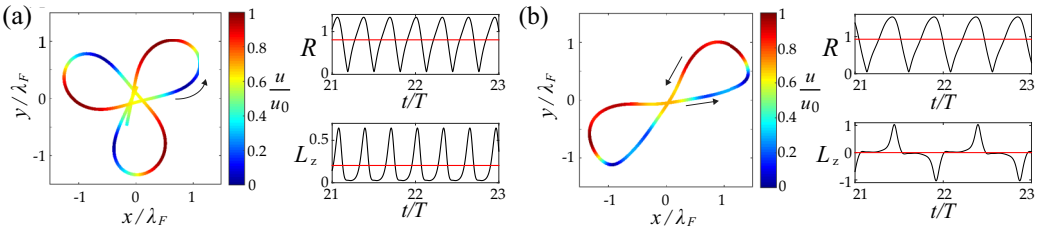

FIG. 2. (a) Example of one period of a quasiperiodic trefoil trajectory for $\gamma/\gamma_F = 0.9448$ under the influence of a harmonic potential with $k = 2.5$ μN/m, corresponding to $\Lambda = 0.5459$. (b) Example of a purely periodic lemniscate trajectory arising for $\gamma/\gamma_F = 0.9516$ and $k = 2.2$ μN/m, corresponding to $\Lambda = 0.5893$. Accompanying panels show the time evolution of the dimensionless distance from the origin R and the dimensionless angular momentum L_z, as defined in Eqs. (3) and (4). Average values are indicated by red lines and u_0 denotes the free-walking speed. Here T is one orbital period. Trajectories are color coded according to walker speed nondimensionalized by the free speed u/u_0. Arrows indicate direction of motion.

$0.94 < \gamma/\gamma_F < 0.97$, various periodic and quasiperiodic trajectories arise prior to the transition to chaos. For larger $k > 3$ μN/m, the transition from circular to chaotic trajectories is relatively abrupt. The range $0.1 \leqslant k \leqslant 5.8$ μN/m was sufficient to capture a variety of quasiperiodic and chaotic trajectories.

The dashed curve in Fig. 1 corresponds to $\sqrt{m/k} = T_d/(1 - \gamma/\gamma_F)$. Above this curve the characteristic crossing or orbital time $T_s = \sqrt{m/k}$ is less than the memory time $T_M = T_d/(1 - \gamma/\gamma_F)$, so the drop is influenced by waves generated along the entirety of its last crossing or orbit. We note also that for $k \gtrsim 4mu_0^2/\lambda_F^2 \approx 3.6$ μN/m, the range of the drop $R = u_0\sqrt{m/k}$ is generally less than the characteristic structure of the wave field $\lambda_F/2$, eliminating the possibility of the orbital structure required for double quantization. We proceed by presenting a detailed account of the various trajectories observed numerically in Fig. 1.

IV. PERIODIC AND QUASIPERIODIC TRAJECTORIES

The most prevalent trajectories reported in the experiments corresponded to circles, trefoils, and lemniscates [13]. The parameter regimes in which these trajectories were observed in our numerical simulations are indicated in Fig. 1. We define quasiperiodic trajectories as those whose structure rotates about the center, corresponding to a periodic motion with a precessional component, an example being the trefoil evident in Fig. 2(a). We define chaotic trajectories as those arising following the Ruelle-Takens-Newhouse-type transition to chaos characterized by Tambasco *et al.* [28]. Figure 2 shows examples of trefoil and lemniscate trajectories along with the time evolution of the corresponding nondimensional radius $R = |\boldsymbol{x}_p|/\lambda_F$ and nondimensional angular momentum $L_z = (\boldsymbol{x}_p \times \dot{\boldsymbol{x}}_p)/V\lambda_F$ over several orbital periods T, as well as their mean values $\overline{R}$ and $\overline{L_z}$.

Figure 3 shows several examples of periodic and quasiperiodic trajectories found numerically. The trajectory in Fig. 3(a) is an elliptic orbit corresponding to the orange circles in Fig. 1. Trajectories shown in Figs. 3(b)–3(d) were not reported in the experiments [13] and exist only in very limited regions of parameter space (see Fig. 1). We note that the trajectory in Fig. 3(b) can be thought of as a period-doubled realization of a lemniscate (Fig. 1, red) and that in Fig. 3(c) as a period-doubled realization of Fig. 3(b). The droplet speed is seen to vary by approximately 60% along the trajectories, suggesting that the assumption of constant speed in the calculations of Perrard *et al.* [13] may not have been entirely justified. Generally, the walker slows down as it approaches an extremity in radius and then accelerates towards the center as its potential energy is converted into kinetic energy. We next explore the nature of the quantization in mean radial extent and mean angular momentum for these periodic trajectories.

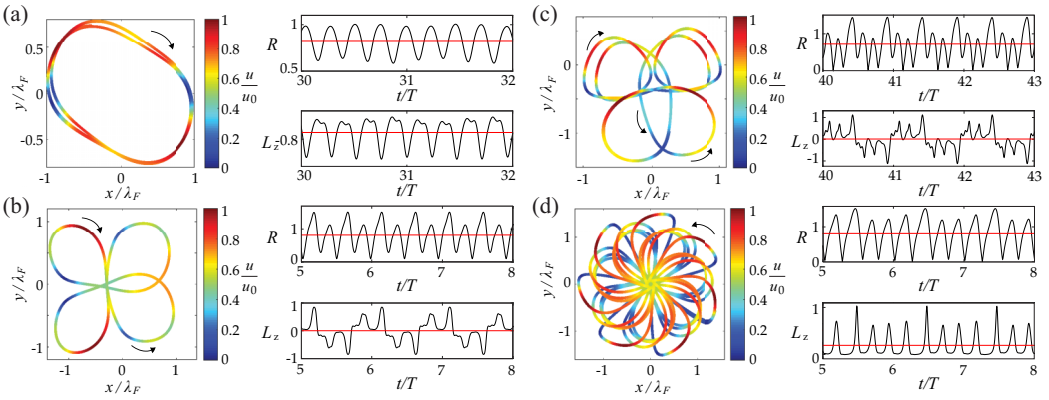

FIG. 3. Periodic and quasiperiodic trajectories found numerically. Trajectories are color coded according to the walker speed $u(t)$. Accompanying panels show the evolution of the dimensionless orbital radius R and angular momentum L_z of each trajectory; T is the orbital period for each trajectory. The horizontal red lines denote mean values of each quantity and u_0 denotes the free-walking speed of a straight-line walker. The relevant parameter values for each trajectory are as follows: (a) $\gamma/\gamma_F = 0.9618$, $k = 1.9$ μN/m, and $\Lambda = 0.6962$; (b) $\gamma/\gamma_F = 0.9595$, $k = 2.2$ μN/m, and $\Lambda = 0.6227$; (c) $\gamma/\gamma_F = 0.9664$, $k = 2.2$ μN/m, and $\Lambda = 0.6413$; and (d) $\gamma/\gamma_F = 0.9459$, $k = 2.8$ μN/m, and $\Lambda = 0.4983$. Arrows indicate direction of motion.

V. QUANTIZATION OF MEAN RADIUS AND ANGULAR MOMENTUM

We first explore the extent to which quantization of the mean radius and angular momentum of periodic and quasiperiodic trajectories is recovered by our numerical model. We then apply the methodology introduced by Durey and Milewski [26] to elucidate the statistical structure emerging in the chaotic regime.

Using the same color scheme as in the regime diagram, Fig. 4 shows the relationship between mean radius and mean angular momentum [defined, respectively, in Eqs. (3) and (4)] for all periodic

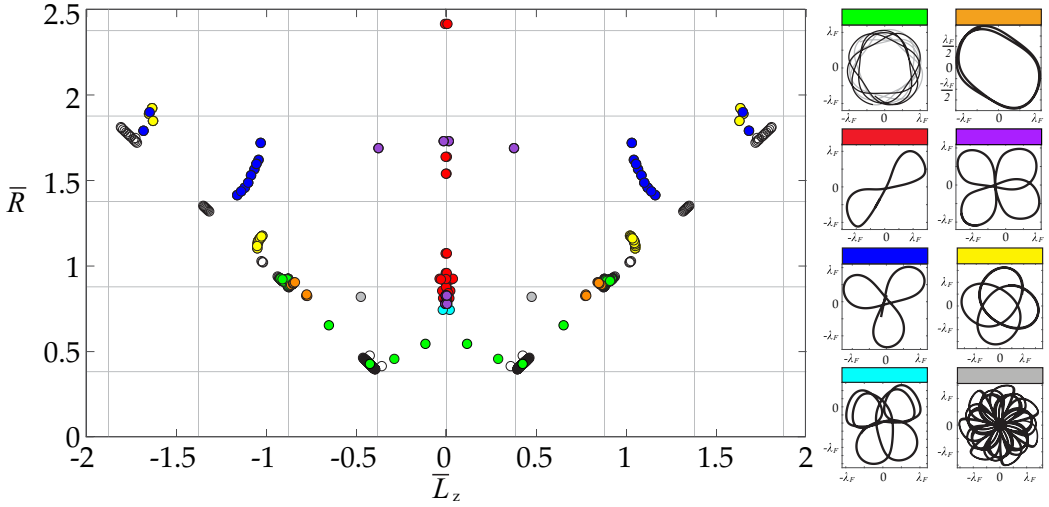

FIG. 4. Dimensionless mean radius $\overline{R}$ and mean angular momentum $\overline{L}_z$ for the periodic and quasiperiodic trajectories observed for $\gamma/\gamma_F > 0.95$. The linear stability analysis of Labousse *et al.* [14] demonstrates that quantization is largely absent for lower values of γ/γ_F. Data have been symmetrized about $\overline{L}_z = 0$.

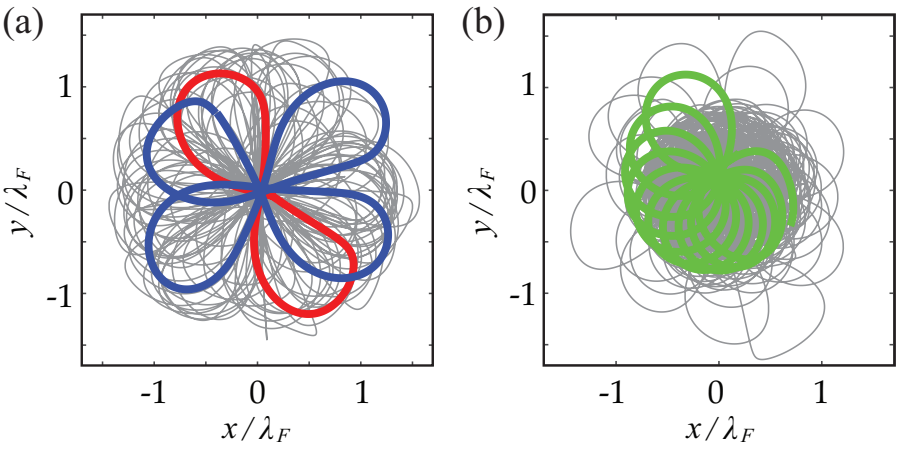

FIG. 5. Decomposition of chaotic trajectories into quasiperiodic components. The trajectories arise for (a) $\gamma/\gamma_F = 0.9470$, $k = 3$ μN/m, and $\Lambda = 0.4717$ and (b) $\gamma/\gamma_F = 0.9675$, $k = 3$ μN/m, and $\Lambda = 0.5733$. In (a), a lemniscate (red) and period-doubled lemniscate (blue) are apparent, while a drifting loop (green) is apparent in (b).

and quasiperiodic orbital trajectories observed in the region of parameter space with $\gamma/\gamma_F > 0.95$. We choose this range of γ/γ_F as quantization of circular orbits is not present for lower values of memory [14]. The horizontal grid lines correspond to the successive zeros of $J_0(k_F r)$ that roughly correspond to the radii of stable circular orbits [14]. In the approximation $|\dot{\boldsymbol{x}}_p| \sim V$, which is valid for circular orbits, Eq. (4) implies that $\overline{L}_z \sim \overline{R}$; consequently, we also choose the vertical grid lines corresponding to the successive zeros of $J_0(k_F r)$.

Note that circular orbits, depicted on the diagram by black open circles, are quantized in both mean radius and angular momentum, which is consistent with the linear stability analysis of circular orbits [14]. By symmetry, lemniscate trajectories (red) have approximately zero mean angular momentum, which is also evident in Fig. 2(b). Lemniscates appear in two main groups, though they are less sharply quantized in $\overline{R}$ than circular orbits. As in the laboratory experiments [13], trefoil trajectories are confined to a limited region in the $(\overline{L}_z, \overline{R})$ plane. The data for trefoils explore a narrow range of values in $\overline{L}_z$ but are spread out in $\overline{R}$, suggesting a sharper quantization in mean angular momentum

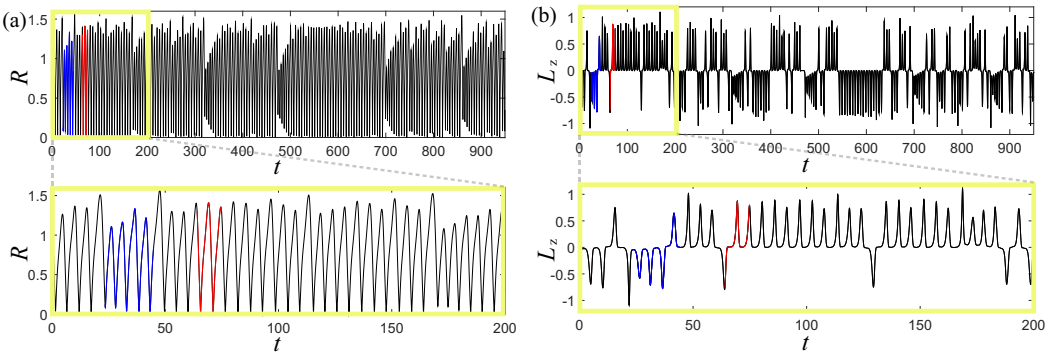

FIG. 6. Time series of (a) the dimensionless orbital radius R and (b) the dimensionless angular momentum L_z for the chaotic trajectory in Fig. 5(a) with $\gamma/\gamma_F = 0.9470$, $k = 3$ μN/m, and $\Lambda = 0.4717$. The red and blue portions in each panel correspond to the red and blue path segments highlighted in Fig. 5(a). The yellow boxes are expanded below.

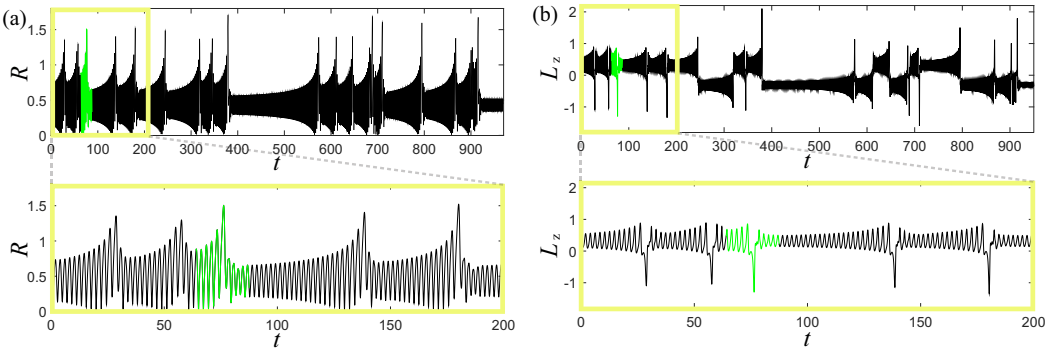

FIG. 7. Time series of (a) the dimensionless orbital radius R and (b) the dimensionless angular momentum L_z for the chaotic trajectory in Fig. 5(b) with $\gamma/\gamma_F = 0.9675$, $k = 3\ \mu$N/m, and $\Lambda = 0.5733$. The green portion in each panel corresponds to the green section highlighted in Fig. 5(b). The yellow boxes are expanded below.

than in mean radial extent. The groupings of data for the other trajectories show similar behavior with the exception of wobbling trajectories (green), which exhibit considerable scatter in both quantities.

For high forcing acceleration ($\gamma/\gamma_F > 0.975$), predominantly chaotic trajectories are observed for a wide range of spring constants k. As in the experiments [13], unstable periodic and quasiperiodic orbits could be identified within chaotic trajectories (Fig. 5), suggesting the presence of some coherent underlying statistical behavior. Specifically, in Fig. 5(a), we identify a lemniscate (red) and period-doubled lemniscate (blue), while in Fig. 5(b), a drifting precessing loop is apparent within the chaotic trajectory. Figure 6(a) shows the time series of the orbital radius from the trajectory shown in Fig. 5(a), while Fig. 6(b) shows the corresponding angular momentum. Figure 6(a) shows the rapid variations in radius while Fig. 6(b) highlights the trajectory's chaotic switching between clockwise ($L_z < 0$) and counterclockwise ($L_z > 0$) paths. A similar set of time series shown in Fig. 7 corresponds to the trajectory in Fig. 5(b).

For a given chaotic path, we follow Durey and Milewski [26] in defining subtrajectories as segments of the total trajectory arising between successive local maxima in radius $|\boldsymbol{x}_p(t)|$ and weight each subtrajectory by its number of time steps. We note that such subtrajectories are generally different for each type of periodic or quasiperiodic trajectory. For example, between successive maxima of a stable lemniscate, one obtains two segments, each with zero average angular momentum. Conversely, subtrajectories of a stable trefoil correspond to three identical segments of nonzero average angular momentum [26]. This classification allows us to decompose the chaotic trajectories into subtrajectories associated with the periodic and quasiperiodic trajectories of Fig. 4. A visual description of our methodology for defining subtrajectories is given in Fig. 8. The complete trajectory is plotted in gray, while several subtrajectories are plotted in an alternating pattern of red and green. The color along the trajectory changes whenever a local maximum in radial extent $|\boldsymbol{x}_p(t)|$ is achieved. Along each such segment, the mean radius $\overline{R}$ and mean angular momentum $\overline{L}_z$ are calculated. Each subtrajectory then corresponds to a single data point in the $(\overline{L}_z, \overline{R})$ plane, denoted by blue circles in Fig. 8(b). The red data points in Fig. 8(b) denote the centroids of the resulting clusters deduced using the K-means clustering algorithm [26], which minimizes the Euclidean distance between points in each cluster given a prescribed number of clusters K [35,36].

With a view to quantifying the effect shown in Fig. 5, we follow Durey and Milewski [26] in applying the K-means clustering algorithm to subtrajectories within the chaotic regime. The appropriate value for K can typically be determined by direct observation as in Fig. 8(b). To do this rigorously, several statistical techniques are available to identify an optimal K value, of which we use the silhouette method [36,37]. This method introduces the silhouette width, which quantifies both the tightness of each cluster and its separation from other clusters [37]. To identify the best number of clusters K to use for a given data set, we use the value of K in the interval $1 \leqslant K \leqslant 6$ that

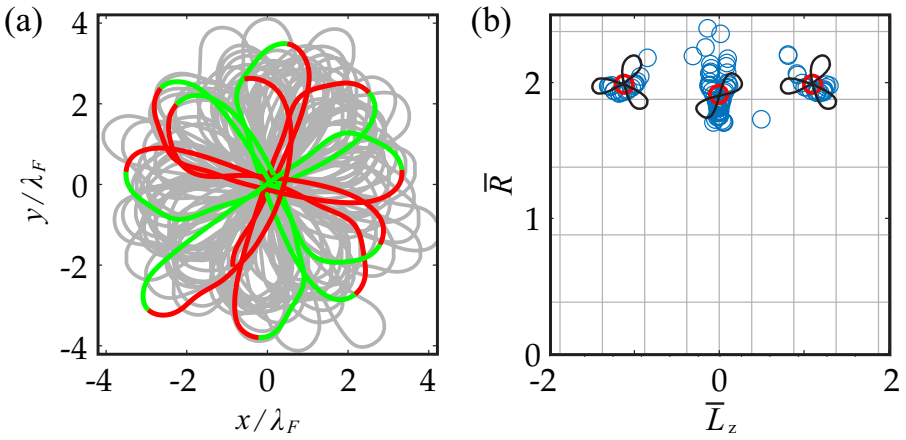

FIG. 8. (a) A chaotic trajectory is sliced into successive red and green subtrajectories. The color along the trajectory changes from red to green or vice versa whenever a local maximum in radial extent $|\boldsymbol{x}_p(t)|$ is achieved. Here $\gamma/\gamma_F = 0.971$, $k = 0.74\ \mu$N/m, and $\Lambda = 1.132$. (b) Example of clustered data from subtrajectories along the chaotic trajectory in (a). Each blue circle, an $(\overline{L}_z, \overline{R})$ pair, corresponds to a particular subtrajectory. Each red circle denotes the centroid of a cluster determined using the K-means algorithm. The overlying trajectories in black correspond to the periodic and quasiperiodic states shown in Fig. 4. The grid lines are the same as those used in Fig. 4.

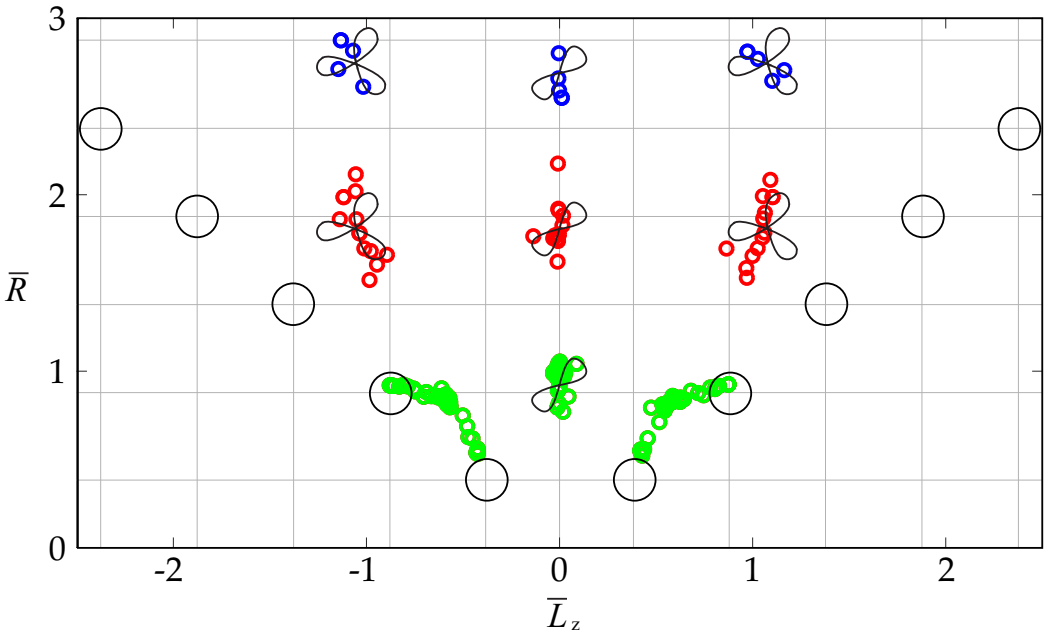

FIG. 9. Shown in green, red, and blue are centroids of clusters for chaotic trajectories at $\gamma/\gamma_F = 0.971$, for spring constants in the range $0.1 \leqslant k \leqslant 5.8\ \mu$N/m, with corresponding Λ in the range $0.3986 \leqslant \Lambda \leqslant 3.254$. The blue, red, and green markers denote spring constants in the ranges $k < 0.57\ \mu$N/m, $0.57 \leqslant k < 1.36\ \mu$N/m, and $k \geqslant 1.36\ \mu$N/m, respectively.

maximizes the average silhouette width. Figure 8 shows an example of K-means clustering where $K = 3$ yielded the largest average silhouette width.

Figure 9 is a collection of such centroids from chaotic trajectories arising at fixed forcing acceleration $\gamma/\gamma_F = 0.971$ and with spring constant varying over the range $0.1 \leqslant k \leqslant 5.8$ μN/m, corresponding to the range explored in the regime diagram. The trajectories that produced centroids with largest average radii correspond to small spring constants: As the spring constant is increased progressively, the central force prohibits the droplet from walking far from the origin. Specifically, the blue, red, and green markers denote spring constants in the ranges $k < 0.57$ μN/m, $0.57 \leqslant k < 1.36$ μN/m, and $k \geqslant 1.36$ μN/m, respectively. Note that the centroids cluster in distinct groups. This grouping suggests that, while the individual trajectories exhibit chaotic behavior, an underlying statistical structure is present, reflecting the dynamic constraint imposed on the droplet by its pilot-wave field. The black trajectories identify the periodic base states within the chaotic trajectories and roughly correspond to the locations of those in Fig. 4.

For smaller spring constants than considered here, one might assume that the vertical axis in Fig. 9 could be extended to larger values of $\overline{R}$ to reveal more clusters; however, such is not the case. The double quantization emerges as a result of the competition between the the spring force and the wave force. When the spring constant becomes small, the range of drop motion or orbital radius $R \sim u_0\sqrt{m/k}$ becomes large. The characteristic time scale of the walker's trajectory $T_s = \sqrt{m/k}$ may then exceed the memory time $T_M = T_d/(1 - \gamma/\gamma_F)$. The dashed line in Fig. 1 denotes the locus of the curve $T_s = T_M$ above which the drop is influenced by waves generated along the entirety of its last crossing or orbit. We note that the orbital structure associated with the double quantization is also precluded at large k, when the range R becomes less than the characteristic scale of the wave field $\lambda_F/2$. Specifically, $k \gtrsim 4mu_0^2/\lambda_F^2 \approx 3.6$ μN/m in Fig. 1.

VI. DISCUSSION

We have numerically simulated an integro-differential trajectory equation that describes the horizontal motion of a walker in a harmonic potential. Our results are summarized in a regime diagram (Fig. 1) that illustrates the dependence of the form of the walker's trajectory on system parameters. We obtain trajectories similar to those reported in the laboratory experiments of Perrard *et al.* [13], including circles, trefoils, lemniscates, and ellipses. We also find trajectories that were not reported, such as those shown in Fig. 3. We note that these trajectories were found in relatively narrow regions of parameter space and can be viewed as period-doubled versions of experimentally observed trajectories.

While the numerical simulations recovered qualitative features of the experiments, quantitative discrepancies still remain. These may arise from model failings in the high-memory regime where chaotic bouncing states may arise, so the assumption of a period-doubled walking state may be invalid and phase changes in the walker's vertical dynamics may become dynamically significant [31,38]. Another possible source of discrepancy with the experimental results is the experimental variability in drop size. The drop size used in experiments was not reported, which may have introduced errors in the reported values of $\overline{L}_z$. In addition, the potential used in the experiments was approximated to be harmonic up to $\sim 3\lambda_F$, whereas we impose a harmonic potential everywhere in the simulations. This may lead to discrepancies in the form of the far-field potential and hence the droplet dynamics.

We also conducted a series of simulations aimed at characterizing the sensitivity of our system to both the assumed form of the wave field and the system parameters. First, we examined the influence of spatial damping on the system behavior by running simulations for a wave field (2) without the spatial damping term. While quantitative differences in the resulting regime diagram relative to Fig. 1 arose, the general behavior was similar, with analogous periodic and quasiperiodic trajectories emerging at low memory and double quantization in the high-memory chaotic regime. Similarly, running simulations for a different drop size ($R_d = 0.4$ mm) yielded qualitatively similar results. We thus conclude that the gross features elucidated herein, particularly the double quantization emerging

in the chaotic regime, are not peculiar to the specific parameter regime or wave model considered, but are rather a robust feature of pilot-wave hydrodynamics in a simple harmonic potential.

We note that the two-dimensional quantum harmonic oscillator exhibits a particular double quantization in energy E and angular momentum L_z. Specifically, for a given spring constant k and associated vibrational frequency $\omega = \sqrt{k/m}$, the stationary states have $E = (n+1)\hbar\omega$ and $L_z = j\hbar$, where n is a non-negative integer and $j = -n, -n+2, \ldots, n-2, n$. That is, different quantized energy levels may be accessed for a fixed value of the spring constant and the corresponding angular momenta $|L_z| \leqslant E/\omega$ are quantized in steps of $2\hbar$. The quantization of mean radial extent and mean angular momentum in our system is different, owing to the fact that a walker has a prescribed free walking speed u_0. A walker's radial extent is roughly prescribed by the balance of centripetal acceleration mu_0^2/R and restoring force kR, so $R \sim u_0/\omega$ in the walker system; consequently, it is necessary to vary the spring constant k in order to realize different values of R.

The double quantization arises for periodic orbits when the memory time exceeds the characteristic orbital period and when the orbital range exceeds the characteristic scale of the wave field. Similarly, in the chaotic regime, the memory time must exceed the characteristic crossing time. The trajectories can then be decomposed into unstable quasiperiodic trajectories along with intermittent transients. Our study provides further evidence for the manner in which a coherent statistics may emerge from chaotic pilot-wave dynamics in a central force, as was suggested in the original studies [13,24] and by the recent work of Durey and Milewski [26].

The chaotic trajectories in our system seem to be approximately quantized according to the rule $(\overline{L}_z, \overline{R}) = (j,n)$, where $j = -1,0,1$ and $n = 1,2,3$, which is different from the double quantization of energy and angular momentum in the two-dimensional quantum harmonic oscillator. Durey and Milewski [26] (see Fig. 12 therein) observed similar clusters to ours for $n = 1$ and 2, but not for $n = 3$. They also observed clusters for $\overline{R} = \overline{L}_z = 1.5$ and $\overline{R} = \overline{L}_z = 2.5$, corresponding to circular arcs that were not observed in our simulations. However, they failed to observe clusters at other half-integer values of $\overline{R}$ and $\overline{L}_z$. While the gross features of the double quantization reported in the experiments of Perrard *et al.* [13] have been captured by the results of both Durey and Milewski [26] and our study, these theoretical studies suggest that the details of the double quantization observed in this hydrodynamic pilot-wave system are sensitive to the specifics of the wave model. The possibility remains that a sharper, more quantumlike quantization may emerge in a different pilot-wave system.

In future work, one may apply the methodology of Durey and Milewski [26] followed here to the chaotic trajectories of walkers under the influence of a Coriolis force [12,23,39] with a view to seeking a similar double quantization in that system. A broader exploration of pilot-wave systems with different external forces and geometries should yield a better understanding of the emergent statistics of chaotic pilot-wave dynamics.

ACKNOWLEDGMENTS

The authors gratefully acknowledge Matt Durey, Paul Milewski, and Ruben Rosales for valuable input. J.B. gratefully acknowledges the financial support of the NSF through Grants No. CMMI-1333242 and No. DMS-1614043. A.O. acknowledges the support of the NSF Mathematical Sciences Postdoctoral Research Fellowship, with the associated Grant No. DMS-1400934. K.K. acknowledges financial support from NSF Graduate Research Fellowship Primary Award No. 1122374.

[1] Y. Couder, E. Fort, C.-H. Gautier, and A. Boudaoud, From Bouncing to Floating: Noncoalescence of Drops on a Fluid Bath, Phys. Rev. Lett. **94**, 177801 (2005).

[2] M. Faraday, On a peculiar class of acoustical figures, and on certain forms assumed by groups of particles upon vibrating elastic surfaces, Philos. Trans. R. Soc. London **121**, 299 (1831).

[3] Y. Couder, S. Protière, E. Fort, and A. Boudaoud, Dynamical phenomena: Walking and orbiting droplets, Nature (London) **437**, 208 (2005).

[4] S. Protière, A. Boudaoud, and Y. Couder, Particle-wave association on a fluid interface, J. Fluid Mech. **554**, 85 (2006).
[5] A. Eddi, E. Sultan, J. Moukhtar, E. Fort, M. Rossi, and Y. Couder, Information stored in Faraday waves: The origin of a path memory, J. Fluid Mech. **674**, 433 (2011).
[6] Y. Couder and E. Fort, Single-Particle Diffraction and Interference at a Macroscopic Scale, Phys. Rev. Lett. **97**, 154101 (2006).
[7] A. Andersen, J. Madsen, C. Reichelt, S. Ahl, B. Lautrup, C. Ellegaard, M. Levinsen, and T. Bohr, Double-slit experiment with single wave-driven particles and its relation to quantum mechanics, Phys. Rev. E **92**, 013006 (2015).
[8] A. Eddi, E. Fort, F. Moisy, and Y. Couder, Unpredictable Tunneling of A Classical Wave-Particle Association, Phys. Rev. Lett. **102**, 240401 (2009).
[9] A. Nachbin, P. A. Milewski, and J. W. M. Bush, Tunneling with a hydrodynamic pilot-wave model, Phys. Rev. Fluids **2**, 034801 (2017).
[10] E. Fort, A. Eddi, A. Boudaoud, J. Moukhtar, and Y. Couder, Path-memory induced quantization of classical orbits, Proc. Natl. Acad. Sci. USA **107**, 17515 (2010).
[11] A. U. Oza, D. M. Harris, R. R. Rosales, and J. W. M. Bush, Pilot-wave dynamics in a rotating frame: On the emergence of orbital quantization, J. Fluid Mech. **744**, 404 (2014).
[12] D. M. Harris and J. W. M. Bush, Droplets walking in a rotating frame: From quantized orbits to multimodal statistics, J. Fluid Mech. **739**, 444 (2014).
[13] S. Perrard, M. Labousse, M. Miskin, E. Fort, and Y. Couder, Self-organization into quantized eigenstates of a classical wave-driven particle, Nat. Commun. **5**, 3219 (2014).
[14] M. Labousse, A. U. Oza, S. Perrard, and J. W. M. Bush, Pilot-wave dynamics in a harmonic potential: Quantization and stability of circular orbits, Phys. Rev. E **93**, 033122 (2016).
[15] D. M. Harris, J. Moukhtar, E. Fort, Y. Couder, and J. W. M. Bush, Wavelike statistics from pilot-wave dynamics in a circular corral, Phys. Rev. E **88**, 011001(R) (2013).
[16] T. Gilet, Dynamics and statistics of wave-particle interactions in a confined geometry, Phys. Rev. E **90**, 052917 (2014).
[17] T. Gilet, Quantumlike statistics of deterministic wave-particle interactions in a circular cavity, Phys. Rev. E **93**, 042202 (2016).
[18] D. M. Harris and J. W. M. Bush, The pilot-wave dynamics of walking droplets, Phys. Fluids **25**, 091112 (2013).
[19] L. de Broglie, Interpretation of quantum mechanics by the double solution theory, Ann. Fond. **12**, 399 (1987).
[20] L. de la Peña, A. M. Cetto, and A. Valdeés Hernández, *The Emerging Quantum: The Physics behind Quantum Mechanics* (Springer, New York, 2014).
[21] J. W. M. Bush, Pilot-wave hydrodynamics, Annu. Rev. Fluid Mech. **47**, 269 (2015).
[22] J. W. M. Bush, The new wave of pilot-wave theory, Phys. Today **68(8)**, 47 (2015).
[23] A. U. Oza, Ø. Wind-Willassen, D. M. Harris, R. R. Rosales, and J. W. M. Bush, Pilot-wave dynamics in a rotating frame: Exotic orbits, Phys. Fluids **26**, 082101 (2014).
[24] M. Labousse, S. Perrard, Y. Couder, and E. Fort, Build-up of macroscopic eigenstates in a memory-based constrained system, New J. Phys. **16**, 113027 (2014)
[25] S. Perrard, M. Labousse, E. Fort, and Y. Couder, Chaos Driven by Interfering Memory, Phys. Rev. Lett. **113**, 104101 (2014).
[26] M. Durey and P. A. Milewski, Faraday wave-droplet dynamics: Discrete-time analysis, J. Fluid Mech. **821**, 296 (2017).
[27] A. U. Oza, E. Siéfert, D. M. Harris, J. Moláček, and J. W. M. Bush, Orbiting pairs of walking droplets: Dynamics and stability, Phys. Rev. Fluids **2**, 053601 (2017).
[28] L. D. Tambasco, D. M. Harris, A. U. Oza, R. R. Rosales, and J. W. M. Bush, The onset of chaos in orbital pilot-wave dynamics, Chaos **26**, 103107 (2016).
[29] A. U. Oza, R. R. Rosales, and J. W. M. Bush, A trajectory equation for walking droplets: Hydrodynamic pilot-wave theory, J. Fluid Mech. **737**, 552 (2013).
[30] J. Moláček and J. W. M. Bush, Drops bouncing on a vibrating bath, J. Fluid Mech. **727**, 582 (2013).

[31] J. Moláček and J. W. M. Bush, Droplets walking on a vibrating bath: towards a hydrodynamic pilot-wave theory, J. Fluid Mech. **727**, 612 (2013).
[32] P. A. Milewski, C. A. Galeano-Rios, A. Nachbin, and J. W. M. Bush, Faraday pilot-wave hydrodynamics: Modelling and computation, J. Fluid Mech. **778**, 361 (2015).
[33] F. Blanchette, Modeling the vertical motion of drops bouncing on a bounded fluid reservoir, Phys. Fluids. **28**, 032104 (2016).
[34] A. P. Damiano, P.-T. Brun, D. M. Harris, C. A. Galeano-Rios, and J. W. M. Bush, Surface topography measurements of the bouncing droplet experiment, Exp. Fluids **57**, 163 (2016).
[35] J. A. Hartigan, *Clustering Algorithms* (Wiley, New York, 1975).
[36] J. A. Hartigan and M. A. Wong, A K-means clustering algorithm, J. R. Stat. Soc. Ser. C **28**, 100 (1979).
[37] T. M. Kodinariya and P. R. Makwana, Review on determining number of cluster in K-means clustering, Int. J. Adv. Res. Comput. Sci. Manag. Stud. **1**, 90 (2013).
[38] Ø. Wind-Willassen, J. Moláček, D. M. Harris, and J. W. M. Bush, Exotic states of bouncing and walking droplets, Phys. Fluids **25**, 082002 (2013).
[39] S. Protière, S. Bohn, and Y. Couder, Exotic orbits of two interacting wave sources, Phys. Rev. E **78**, 036204 (2008).